ARTIFICIAL INTELLIGENCE CONTROL OF A TURBULENT JET

Dewei Fan
Institute for Turbulence-Noise-Vibration
Interaction and Control
Harbin Institute of Technology (Shenzhen)
People's Republic of China
fandewei2014@hotmail.com

Yu Zhou
Institute for Turbulence-Noise-Vibration
Interaction and Control
Harbin Institute of Technology (Shenzhen)
People's Republic of China
yuzhou@hit.edu.cn

Bernd R. Noack
Institute for Turbulence-Noise-Vibration Interaction and Control
Harbin Institute of Technology (Shenzhen), People's Republic of China
LIMSI, CNRS, Université Paris-Saclay,
Bât 507, rue du Belvédère, Campus Universitaire, F-91403 Orsay, France
bernd.noack@limsi.fr

ABSTRACT

An artificial intelligence (AI) control system is developed to manipulate a turbulent jet targeting maximal mixing. The control system consists of sensors (two hot-wires), genetic programming for evolving the control law and actuators (6 unsteady radial minijets). The mixing performance is quantified by the jet centerline mean velocity. AI control discovers a hitherto unexplored combination of asymmetric flapping and helical forcing. Such a combination of several actuation mechanisms, if not creating new ones, constitutes a large challenge for conventional methods of parametric optimization. AI control vastly outperforms the optimized periodic axisymmetric, helical or flapping forcing produced from conventional open- or closed-loop control. Intriguingly, the learning process of AI control discovers all these forcings in the order of increased performance. Our study is the first AI control experiment which discovers a non-trivial spatially distributed actuation optimizing a turbulent flow. The results show the great potential of AI in conquering the vast opportunity space of control laws for many actuators, many sensors and broadband turbulence.

INTRODUCTION

We present the first turbulence control experiment employing artificial intelligence methods optimizing a spatially distributed actuation. In particular, turbulent jet mixing is optimized by a novel combination of 3D actuation mechanisms learned in situ with linear genetic programming. Turbulence control has a history of thousands of years arguably starting with feathers on an arrow to stabilize it flight from a bow. The first theoretical basis has been established over hundred years ago with the Prandtl's discovery of boundary-layer theory in 1904. Hitherto, most turbulence control studies have either been performed with a direct numerical simulation based on linear control theory or have relied on carefully tuned constant or periodic actuation in experiments (Brunton & Noack, 2015).

In general, active control of jets is divided into open-loop and closed-loop control. Note that closed-loop control shows the potential to significantly reduce power requirements in comparison to open-loop control strategies, since the random aspect of these structures reduces the effectiveness of an open-loop configuration (Moin & Bewley, 1994). Most literature on closed-loop turbulent flow control falls in one of two categories: model-based and model-free tuning of the control laws. For model-based control, the discretised Navier-Stokes equations, reduced-order models and linear stochastic estimation are used to resolve flow physics and nonlinearities (Sipp et al., 2010; Noack et al., 2008). In the previous work (Akervik et al., 2007), reduced-order models were applied to a few non-normal global eigenmodes of the linearized Navier-Stokes equations as a basis for Galerkin projection. Yet, these approaches have limited applicability to unstable advection dominated flows (Onofrio et al., 2011). The model-based control logic is physically appealing but cannot be accurate than the model. However, high-fidely model-based control consumes a large amount of computational time, typically not achievable within the experimental response times. Therefore, model-free control is most widely applied in turbulent flow control. The adaptive PID control was used to suppress cylinder vibration (Zhang et al., 2004). Extremum seeking control (ESC) was used for separation control on a high lift configuration (Becker et al., 2007). Yet, in all reported cases the resulting control law was simple, e.g. based on a single actuator characterizable by one or two parameters. The optimization of such control laws is achievable with conventional techniques (Wu et al., 2018).

The nonlinear control optimization involving many independent actuators can be unimaginably complex. Take the manipulation of a turbulent jet based on unsteady radial minijets for example. One single periodically operated minijet of a given exit diameter may be associated with three control parameters, namely, the excitation frequency f_e, mass flow rate m_{mini} and duty cycle α (Perumal & Zhou, 2018); however, multiple, say six, equally separated independent minijets introduce the complexity of distribut-
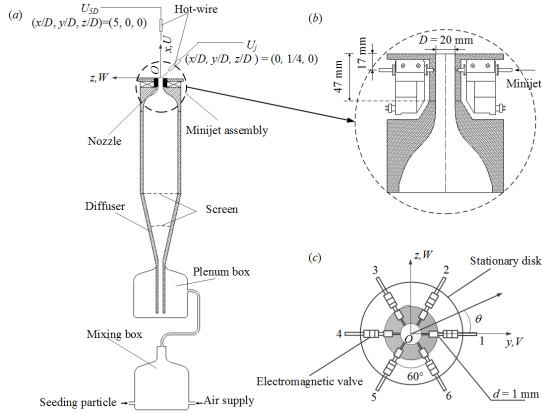
Figure 1. Sketch of the experimental setup: (*a*) main jet facility; (*b*) minijet arrangement; (*c*) minijet assembly.

ed actuation or additional dimensions. The minijets can be active or off and six minijets may occur alternately from one configuration to the other. As a result, the complexity of the problem grows tremendously. The optimization of nonlinear control laws for such high dimension problems is largely terra incognita, which is extremely challenging, if not impossible, for conventional techniques. This is a great challenge for turbulence control. Then could AI be used to control turbulence? Can it outperform conventional methods?

This work aims to answer the above questions. This study focusses on the control of a turbulent jet, one of few best investigated and most complex textbook flows. This configuration has a large range of industrial applications like in inkjet printers, dilution jets in combustors, fuel injection of combustion engines, just to name a few. Another important interest in jet control is noise mitigation (Jordan & Colonius, 2013). The coherent structures of the jet have a large range of scales, varying convection velocity and may feature a rich set of three-dimensional patterns (Garnaud *et al.*, 2013). The control with spatially distributed actuators at the upstream of nozzle exit aims to maximize mixing. Control design is framed as regression problem: find a mapping from inputs, e.g. sensor signals, to outputs, the actuation commands which optimize the cost function. A much richer set of nonlinear control laws has recently been explored with methods of artificial intelligence, like neural networks (Lee *et al.*, 1997), genetic algorithms (Benard *et al.*, 2016) or genetic programming (Duriez *et al.*, 2016). Here following Dracopoulos (1997) and Duriez *et al.* (2016), genetic programming is chosen as a very powerful solver.

EXPERIMENTAL SET-UP

A turbulent round jet facility, including an air supply system, main round jet and minijet actuators is applied. Figure 1(*a*) shows the schematics of the main jet facility. The details are described by Fan *et al.* (2017). The Reynolds number $Re_D = U_j D/\nu$ of the main jet is fixed at 8000, where U_j is the jet centerline velocity measured at the nozzle exit, ν is the kinematic viscosity of air and $D = 20$ mm is the diameter of the nozzle. The centre of the jet exit is set as the origin of a Cartesian coordinate system, where the *x*-axis is aligned with the streamwise direction and the *y*-axis contains minijets No. 1 and No. 4 (figure 1*c*).

The actuation is performed with 6 independent minijets upstream of the nozzle exit. The minijets are connected to six different channels each of which consists of a mass flow meter and flow-limiting valve. The mass flow rate is controlled by the flow-limiting valve and measured by the mass flow meter. The six minijets have orifice diameter of 1 mm are equidistantly placed at $x_i = -0.85 D$, $y_i = (D/2) \cos \theta_i$, $z_i = (D/2) \sin \theta_i$ where $\theta_i = (i-1)2\pi/6$, $i = 1, \ldots, 6$. The locations of the actuators are shown in the figure 1(*b*). The minijets are operated by electromagnetic valves in an ON/OFF mode. The valves limit the frequency of the minijet to 500 Hz, more than three times the characteristic shedding frequency of the unforced jet $f_0 = 135$ Hz and more than seven times the excitation frequency of this study $f_e = 67$ Hz.

The jet exit velocity at $(x/D, y/D, z/D) = (0, -1/4, 0)$ is measured with a tungsten wire of 5 μm in diameter. This hot-wire is operated on a constant temperature circuit (Dantec Streamline) at an overheat ratio of 0.6. The centerline jet velocity at $x/D = 5$ is monitored with a second hot-wire. U_j and U_{5D} denotes the averaged velocities at nozzle exit and after the potential core, respectively. Note that hot-wire is in the plug flow nozzle exit region but slightly of center to allow simultaneous measurements of both quantities in the experiment. The hot-wires are calibrated at the jet exit using a Pitot tube connected to a micromanometer (Furness Controls FCO510). The experimental uncertainty of the hot-wire measurement is estimated to be less than 2%.

A planar high-speed PIV system, including a high speed camera (Dantec Speed Sence90C10, 2056×2056 pixels resolution) and pulsed laser source (Litron LDY304-PIV, Nd:YLF, 120 mJ/pulse) is deployed for flow visualization in the $x-z$, $x-y$ and $y-z$ planes. An oil droplet generator (TSI MCM-30) is used to generate a fog for seeding the flow. The seeding particles are supplied into the mixing chamber (figure 1*a*) to mix with air. Flow illumination is provided by a laser sheet of 1 mm in thickness generated by the pulsed laser via a cylindrical lens. Particle images are captured at a sampling rate of 405 Hz, corresponding to 3 f_0 and 6 f_e.

A *National Instrument* PXIe-6356 multifunction I/O device, connected to a computer, is used in the experiment for the real-time control at a sampling rate of f_{RT}=1 kHz. A LabVIEW Real-Time module is used to execute the program. Commanding actuation and data acquisition are performed at the same sampling rate of 1 kHz. The effective excitation frequency f_e can be expressed by $f_e = f_{RT}/N_{sp}$, where N_{sp} is the number of sampling points in one actuation period $1/f_e$. The working frequency range of actuators ($[0, 500]$ Hz) imposes a minimum value of 2 for N_{sp}. For a given f_e, the possible duty cycles α can be deduced from $\alpha = m/N_{sp}$, $m = 1, \ldots, N_{sp} - 1$. Thus, the number of possible duty cycles N_{sp} decreases with f.

ARTIFICIAL INTELLIGENCE CONTROL
Control Problem and Benchmark Actuations

The jet configuration has 2 hot-wire sensors with signals s_1 and s_2. For the feedback experiment, these hot-wires are moved to $x = 5D$ on the centerline and to $x = 3D$ towards the shear-layer respectively. The sensor signals are comprised in one 2-dimensional column vector $\boldsymbol{s} := [s_1, s_2]^\dagger /U_j$, normalized by the jet velocity. The cost function to be minimized reads $J = \overline{s_1}/U_j = 1 - K$, noting that a reduced centerline velocity implies increased entrainment/mixing in
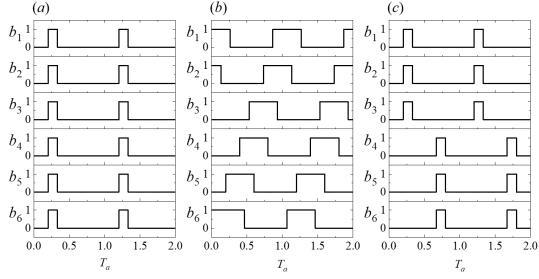
Figure 2. Two periods of the actuation command for the best control laws of generation 1, 2, and 5 of the AI control system. Here, $b_i = 1$ if actuator i is blowing and 0 otherwise.

the potential-core region. The cost has no penalization of actuation as the average mass flow is kept at the same constant for all actuators.

The ith minijet blows if the actuation command b_i command is positive and is closed otherwise. The six-dimensional vector $\boldsymbol{b} = [b_1, \ldots, b_6]^\dagger$ comprises all actuation commands. The actuation may depend on the harmonic functions $h_i = \cos(\omega t - \phi_i)$, $\phi_i = 2\pi i/6$. We use six linearly dependent signals instead of two linearly independent ones to simplify the expressions for helical forcing. The angular frequency ω corresponds to 67 Hz or approximately half the characteristic unforced shedding frequency. This value has been optimized for flapping forcing with a single minijet under the same conditions by Wu *et al.* (2018) and predicted by a global stability analysis Garnaud *et al.* (2013). The six-dimensional vector $\boldsymbol{h} = [h_1, \ldots, h_6]^\dagger$ includes all these harmonic functions. In this notation,

$$\text{axisymmetric} \quad b_i = h_1 - c_a, \quad i = 1, \ldots, 6; \quad (1a)$$

$$\text{helical} \quad b_i = h_i - c_h, \quad i = 1, \ldots, 6; \quad (1b)$$

$$\text{flapping} \quad b_i = h_i - c_f, \quad i = 1, \ldots, 6. \quad (1c)$$

Here, the constants $c_{a,f,h}$ define the duty cycles and have been optimized with respect to the cost. The costs J_a, J_h, J_f of the optimized axisymmetric, helical and flapping forcing constitute the benchmarks for AI control.

Note that three control modes are classified by control signal which have a different phase shift between the any two adjacent minijets (figure 2). Meanwhile, the flow physics of the jet mixing enhancement continues to change as well as the control modes. The details have been discussed below.

Control Optimization using Linear Genetic Programming

Further AI-based jet mixing optimization is based on a general ansatz for periodic open-loop forcing—including the above mentioned forcing:

$$\boldsymbol{b} = \boldsymbol{K}(\boldsymbol{h}). \quad (2)$$

Note that the nonlinear function $\boldsymbol{K}$ can create arbitrary higher harmonics, like the 10th harmonics via $h_1^{10} - 1/2$ as well as arbitrary phase relationships.

The control law (2) is optimized with respect to the cost J using the powerful *linear genetic programming* (L-GP) as a regression solver. We take the same parameters
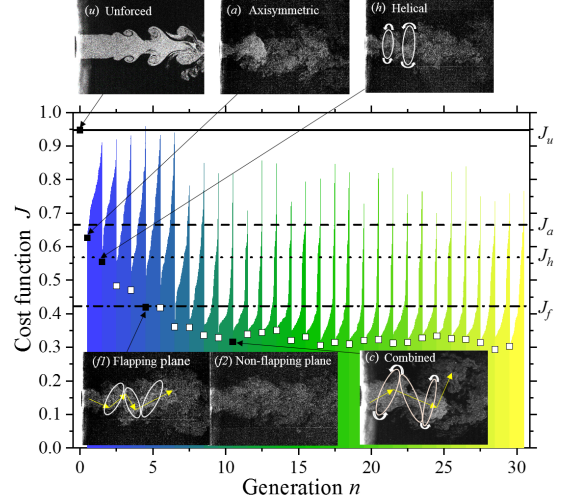

Figure 3. The learning curve of AI control. For details see text.

for control law representation and for the genetic operations as Li *et al.* (2017) for drag reduction of the Ahmed body. The first generation of LGP, $n = 1$, contains $N_i = 100$ random control laws $\boldsymbol{K}_i^1(\boldsymbol{h})$, $i = 1, \ldots, N_i$, also called *individuals*. Each individual is tested for 5 seconds in the experiment to yield the measured cost J_i^1. Subsequent generations are generated from the previous ones with genetic operations (elitism, crossover, mutation and replication) and tested analogously. After the in situ performance measurements, the individuals are re-numbered in order of performance, $J_1^n \leq J_2^n \leq \ldots \leq J_{N_i}^n$, where the superscript 'n' represents the generation number. As plant-specific rule, we discard and replace any individual for testing if one actuator is not active or constant blowing.

RESULTS AND DISCUSSION

Figure 3 displays 3000 evaluated cost functions under AI control. The unforced benchmark cost is marked by an open square at generation 0 and continued as horizontal solid line. The corresponding flow visualization in subfigure (*u*) shows the dye from the nozzle exit in the $x - y$ plane. The displaced vortex rings shed with frequency $f_0 = 135$ Hz.

The following open squares at generation $n = 1, \ldots, 30$ mark the first and best individual of each generation with $N_i = 100$ individuals. The remaining costs of each generation are displayed by the monotonously increasing curve. Every curve has a unique color.

The best individual of the first generation has an axisymmetric control law $b_1 = b_2 = b_3 = b_4 = b_5 = b_6 = -0.832 + \sin(\omega t + 4/6\pi)$. This law is equivalent to (1a) modulo a time shift.

The performance $J_1^1 = 0.626$ is slightly better than the optimized axisymmetric performance (1a). The reason may be attributed to the converged long-term velocity measurement J_a as compared to the short and less accurate measurement of AI control. From several similar or equivalent control laws, only the best value is monitored. It should be noted that learning of AI control only requires an approximately accurate relative ordering of the individuals. An accurate long-term evaluation of the cost is only performed in the last generation $n = 30$. Subfigure (*a*) shows the corre-

sponding flow visualization and the dashed horizontal line represents J_1^1.

In the second generation, AI control discovers the better performing helical forcing $b_1 = \sin(\omega t + 4/6\pi) - 0.145, b_2 = -0.347 \sin \omega t, b_3 = ((\sin(\omega t + 8/6\pi) + (\sin(\omega t + 8/6\pi)^2 + \sin(\omega t + 2/6\pi)^2)) \sin(\omega t + 8/6 * \pi), b_4 = 2\sin(\omega t + 10/6\pi)((\sin(\omega t)^2 - \sin(\omega t + 2/6\pi)(\sin(\omega t)^2 - \sin(\omega t + 2/6\pi)), b_5 = 1/(-0.313 + \sin \omega t) + \sin \omega t), b_6 = -0.354 \sin(\omega t + 8/6\pi)$. This forcing is not of the form (1b), but it clearly shows a uniformly traveling wave in azimuthal direction which is similar to the figure 2(b). The corresponding flow visualization (h) shows a more regular pattern and the cost J_1^2 is marked by a densely dashed horizontal line.

In the fifth generation, AI control learns flapping forcing $b_1 = b_2 = b_3 = -0.811 + \sin(\omega t + 2/6\pi)), b_4 = b_5 = b_6 = -0.782 - \sin(\omega t + 2/6\pi)$. In contrast to (1c), this forcing is asymmetric. An optimized asymmetry yields a reproducibly better mixing. Subfigure (f) shows a strong mixing in the flapping plane(figure 3f1) and a less pronounced mixing in the orthogonal plane (3f2) which is symmetric with respect to the two synchronous actuator groups (figure 2c).

In the eleventh generation, AI control discovers a novel combination of asymmetric flapping forcing and helical forcing, significantly outperforming the flapping forcing of generation $n = 5$ and yielding a decrease of the centerline velocity by more than a factor 3. The corresponding flow visualization (c) indicates the flapping mechanism (compare with (f1)). The helical component will be shown in a later analysis. After this generation, cost and actuation mechanism hardly change in subsequent generations, indicating the convergence of the AI learning process. This actuation mechanism is reproducible, i.e. the combined flapping and helical forcing and very similar cost has been observed in all experiments with different initializations of the first generation. The learning process may not display all of the three symmetric forcings as the best individuals.

The flow response to the four different forcings of AI control is depicted in a near-field cross-plane in figure 4. The first row shows the axisymmetric forcing at 6 consecutive times representing one actuation period. Subfigure (a2) displays the footprint of a vortex ring which disintegrates later in six mushroom-like structures (figure 4 a5,a6). In the second row, helical forcing is clearly evidenced by the clockwise rotating satellite region (figure 4 h1-h6). The third row illustrates flapping flows with patches of dye in the flapping plane (f3,f6) and mushroom-structures at other instances. The bottom row shows the best AI control, combination of asymmetric flapping and helical forcing. The footprints of helical can be seen by the clockwise ring structures (figure 4c1-c6). The flapping component is shown in the figure 3(c) Proximity maps (see § 7-4.1 of Duriez *et al.* (2016)) provide another very revealing illustration of the learning process of the control laws. The underlying metric between two control laws **b** and **b'** is defined as root-mean-square of the Euclidean distance $\sqrt{(1/T)\int_0^T dt \, \|\boldsymbol{b}(t) - \boldsymbol{b}'(t)\|^2}$, $T = 2\pi/\omega$ being the actuation period. Figure 5 displays the proximity map of the control laws in a two-dimensional plane such that this metric is optimally preserved, i.e. close points represent similar control laws. This plane is spanned by the feature coordinates γ_1, γ_2 which are automatically computed from all displayed generations. The associated cost J is color-coded from blue ($J = 0$) to yellow ($J = 1$) as indicated by the colorbar. The subfigures display the feature coordinates of the
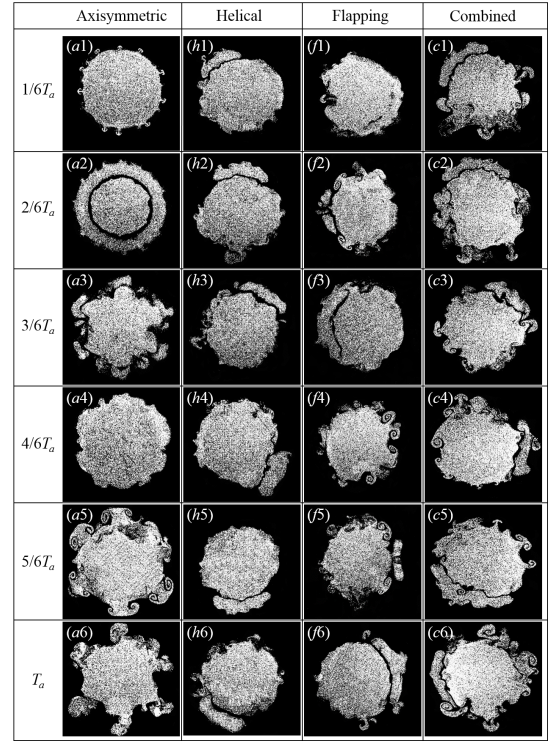

Figure 4. Sequential photographs of the cross-sectional flow structure at $x/D = 0.25$ for the four stages: (a1-a6) axisymmetric forcing, (h1-h6) helical forcing, (f1-f6) flapping forcing, and (c1-c6) combined forcing
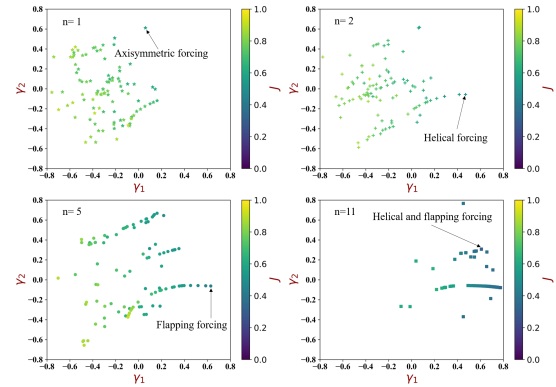

Figure 5. Proximity maps associated with the learning curve (figure 3). The subfigures display the four generations $n = 1, 2, 5, 11$ in which a new actuation mechanism has been learned. Each symbol corresponds to one control law. The best individual has been marked and explained.

four discussed generations. Clearly, the control laws move collectively towards larger γ_1 and lower cost function. Interestingly, the individuals tend to populate discrete curves, a commonly observed phenomenon of AI control.

CONCLUSIONS

An AI control system has been developed which learns automatically how to optimize a spatially distributed actuation and thus a turbulent jet for the targeted cost. Like virtually all control strategies of nonlinear dynamics, AI control solutions do not come with a proof of global optimality.

Yet, the results for jet mixing optimization demonstrate a number of highly desirable features. First, AI control has unveiled a few typical control laws or forcings, i.e., axisymmetric, helical and flapping, in its learning process and eventually converged to a sophisticated spatio-temporal actuation which is the combination of the individual forcings. This combination has produced a fascinating turbulent flow structure characterized by rotating and flapping jet column, along with the generation of mushroom like structures, all acting to enhance jet mixing and thus vastly outperforming several known optimal benchmark actuations. Note that the learning time of 3000 individuals or 6 hours wind-tunnel testing is remarkably short for such a complicated solution. Second, unlike other simple conventional open or closed-loop control methods, AI control could find optimal control laws without any model or assumptions about the actuation mechanisms. Third, the cost J corresponding to AI-learned combination is reproducible with other initial generations. The control laws may analytically differ but produce almost identical actuation commands. Fourth, the parameters of the underlying genetic programming are taken verbatim from (Duriez *et al.*, 2016) and were already proven useful in many other experiments. No sensitive dependence on the parameters has been observed so far and AI control can be expected to yield near-optimal results in its first application to a new plant. The iso-surfaces display flapping and helical motion clearly in the best AI combined forcing. Finally, the search space for a control law is extremely large and of very high complexity / dimensions, including multiple frequencies, minijet configurations, temporal and spatial phase differences between the configurations, and duty cycles of minijets, along with sensor feedback.

ACKNOWLEDGEMENTS

REFERENCES

Akervik, E., Hoepffner, J., Ehrenstein, U. & Henningson, D. S. 2007 Optimal growth, model reduction and control in a separated boundary-layer flow using global eigenmodes. *J. Fluid Mech.* **579** (579), 305–314.

Becker, R., King, R., Petz, R. & Nitsche, W. 2007 Adaptive closed-loop separation control on a high-lift configuration using extremum seeking. *AIAA Journal* **45** (45), 1382–1392.

Benard, N., Pons-Prats, J., Periaux, J., Bugeda, G., Braud, P., Bonnet, J.P. & Moreau, E. 2016 Turbulent separated shear flow control by surface plasma actuator: experimental optimization by genetic algorithm approach. *Exp. Fluids* **57** (2), 22:1–17.

Brunton, S. L. & Noack, B. R. 2015 Closed-loop turbulence control: Progress and challenges. *Appl. Mech. Rev.* **67** (5), 050801:01–48.

Dracopoulos, D. C. 1997 *Evolutionary Learning Algorithms for Neural Adaptive Control*. London, etc.: Springer-Verlag.

Duriez, T., Brunton, S. L. & Noack, B. R. 2016 *Machine Learning Control — Taming Nonlinear Dynamics and Turbulence*, *Fluid Mechanics and Its Applications*, vol. 116. Springer-Verlag.

Fan, D. W., Wu, Z., Yang, H., Li, J. D. & Zhou, Y. 2017 Modified extremum-seeking closed-loop system for jet mixing enhancement. *AIAA Journal* **55** (11), 3891–3902.

Garnaud, X., Lesshafft, L., Schmid, P. J. & Huerre, P. 2013 The preferred mode of incompressible jets: linear frequency response analysis. *J. Fluid Mech.* **716**, 189–202.

Jordan, P. & Colonius, T. 2013 Wave packets and turbulent jet noise. *Ann. Rev. Fluid Mech.* **45**, 173–195.

Lee, C., Kim, J., Babcock, D. & Goodman, R. 1997 Application of neural networks to turbulence control for drag reduction. *Physics of Fluids* **9** (6), 1740–1747.

Li, R., Noack, B. R., Cordier, L., Borée, J. & Harambat, F. 2017 Drag reduction of a car model by linear genetic programming control. *Exp. Fluids* **58**, article 103:1–20.

Moin, P. & Bewley, T. 1994 Feedback control of turbulence. *Annual Review of Fluid Mechanics* **47** (6S).

Noack, B. R., Schlegel, M., Ahlborn, B., Mutschke, G., Morzyński, M., Comte, P. & Tadmor, G. 2008 A finite-time thermodynamics of unsteady fluid flows. *J. Non-Equilibr. Thermodyn.* **33**, 103–148.

Onofrio, S., Shervin, B., Luca, B. & Henningson, D. S 2011 Feedback control of three-dimensional optimal disturbances using reduced-order models. *J. Fluid Mech.* **677** (3), 63–102.

Perumal, A. K. & Zhou, Y. 2018 Parametric study and scaling of jet manipulation using an unsteady minijet. *J. Fluid Mech.* **848**, 592C630.

Sipp, D., Marquet, O.and Meliga, P. & Barbagallo, A. 2010 Dynamics and control of global instabilities in open-flows: A linearized approach. *Appl. Mech. Rev.* **63** (63), 030801.

Wu, Z., Wong, C. W. & Zhou, Y. 2018 Dual-input/single-output extremum-seeking system for jet control. *AIAA Journal* **56** (4), 1463–1471.

Zhang, M. M., Cheng, L. & Zhou, Y. 2004 Closed loop controlled vortex shedding and vibration of a flexibly supported square cylinder under different schemes. *Phys. Fluids* **16** (5), 1439–1448.